Supplemental information

Improvement of sensory deficits in Fragile X mice by increasing cortical interneuron activity after the critical period.

Nazim Kourdougli, Anand Suresh, Benjamin Liu, Pablo Juarez, Ashley Lin, David T. Chung, Anette Graven Sams, Michael Gandal[3] Verónica Martínez-Cerdeño, Dean V. Buonomano, Benjamin J. Hall, Cédric Mombereau, and Carlos Portera-Cailliau*.

Supplementary figures: 13
Supplementary table: 1
Supplementary videos: 2

***Lead Contact:** Carlos Portera-Cailliau

Percentage of PV-tdTom⁺ cells that express GCaMP6S at P15

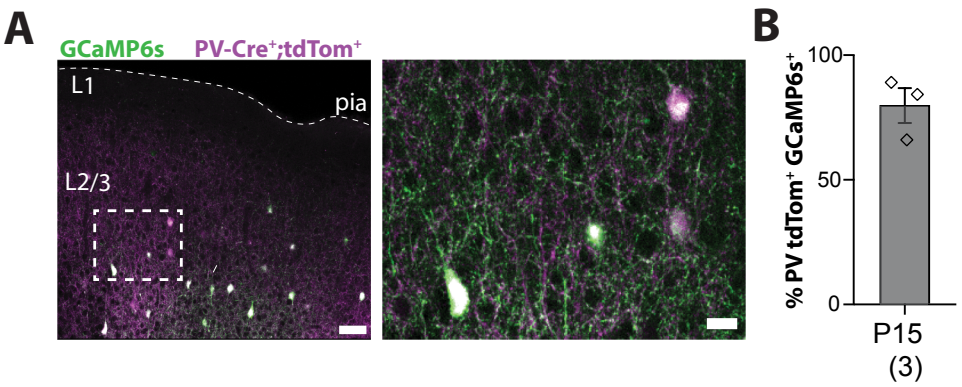

Percentage of Nkx2.1-tdTom⁺ cells that express GCaMP6S at P6

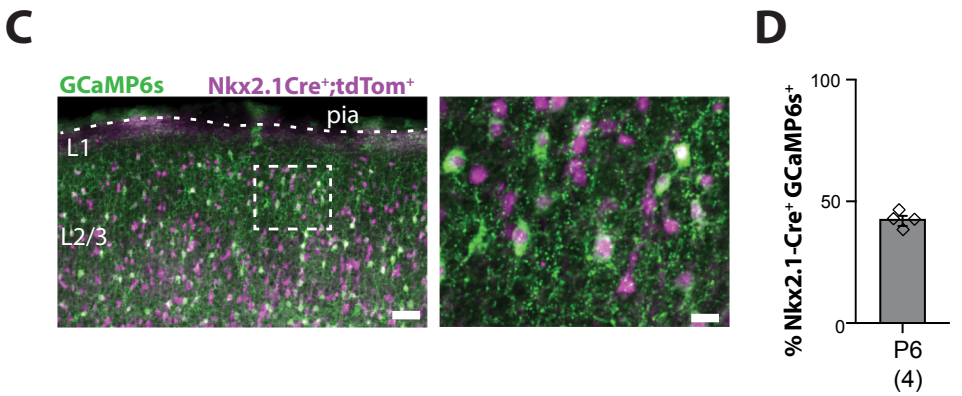

Percentage of Nkx2.1⁺-GCaMP6s⁺ cells that express SST at P6

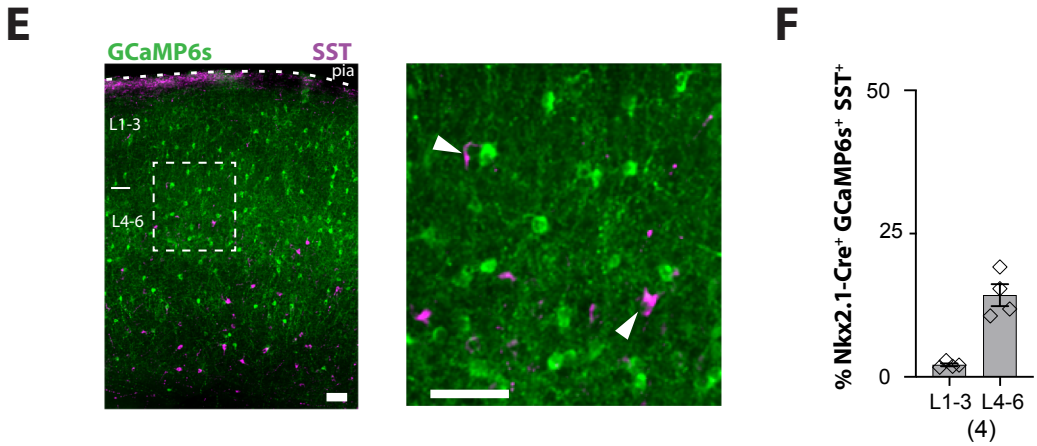

Percentage of Nkx2.1-tdTom⁺ cells that express SST at P6

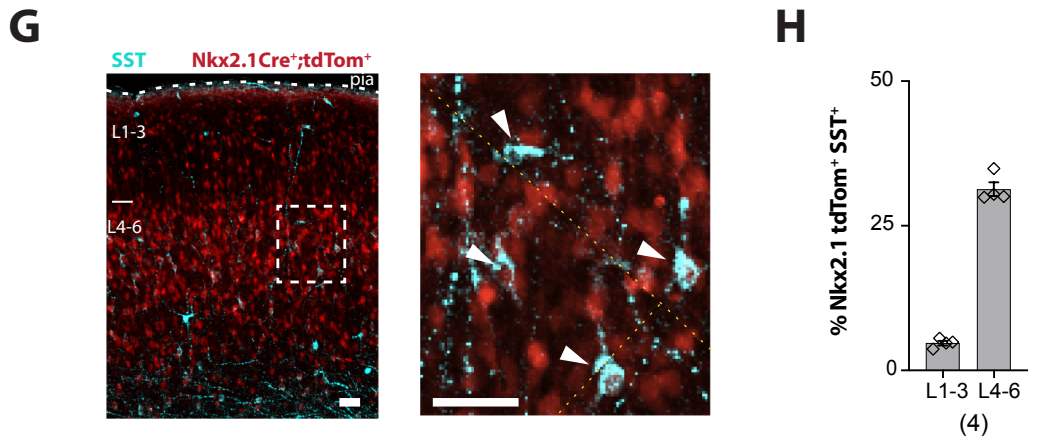

Supplementary Fig. S1

Supplementary Fig. S1: Efficacy of viral strategy to express GCaMP6s in different IN populations in P15 mice. (Related to Fig. 1)

A. Example field of view of PV-Cre^{+}-tdTom^{+} (magenta) expressing GCaMP6s (green) in PV-Cre;Ai14$^{+/-}$*; Fmr1* KO mice at P15.

B. An injection of rAAV-CAG-DIO-GCaMP6s virus in S1 at P10 resulted in a high proportion of PV-INs also expressing GCaMP6s by P15 (79.8± 7%, n=3 mice). This pertains to Fig. 1A-F. Scale= 20 µm.

C. Example field of view of Nkx2.1-Cre^{+}-tdTom^{+} (magenta) expressing GCaMP6s (green) in Nkx2.1-Cre;Ai14$^{+/-}$ *Fmr1* KO mice at P15.

D. An injection of rAAV-CAG-DIO-GCaMP6s virus in S1 at P1 resulted in 43.4± 1.6% of Nkx2.1-INs also expressing GCaMP6s (n=4 mice). Note that the density of Nkx2.1-Cre^{+}- GCaMP6s+ cells is comparable to other reports[1]. This pertains to Fig. 1G-L. Scale= 20 µm.

E. Representative image of Nkx2.1-INs expressing GCaMP6s (arrowheads, following injection of rAAV-CAG-DIO-GCaMP6s virus in S1 at P1) and immunostained for SST at P6. Scale= 50 µm.

F. Percentage of Nkx2.1-Cre^{+};GCaMPs^{+} INs that co-express SST at P6 (2.1± 0.2% in L1-L3 and 14.2± 1.9% in L4-6).

G. Representative image of Nkx2.1-Cre^{+};tdTom^{+} INs immunostained for SST at P6. Arrowheads depicts the co-expressing cells. Yellow dotted line indicates uneven stitching by Zeiss Apotome. Scale= 50 µm.

H. Percentage of Nkx2.1-Cre^{+};tdTom^{+} INs that co-express SST at P6 (4.7± 0.3% in L1-L3 and 31.3± 1.2% in L4-6).

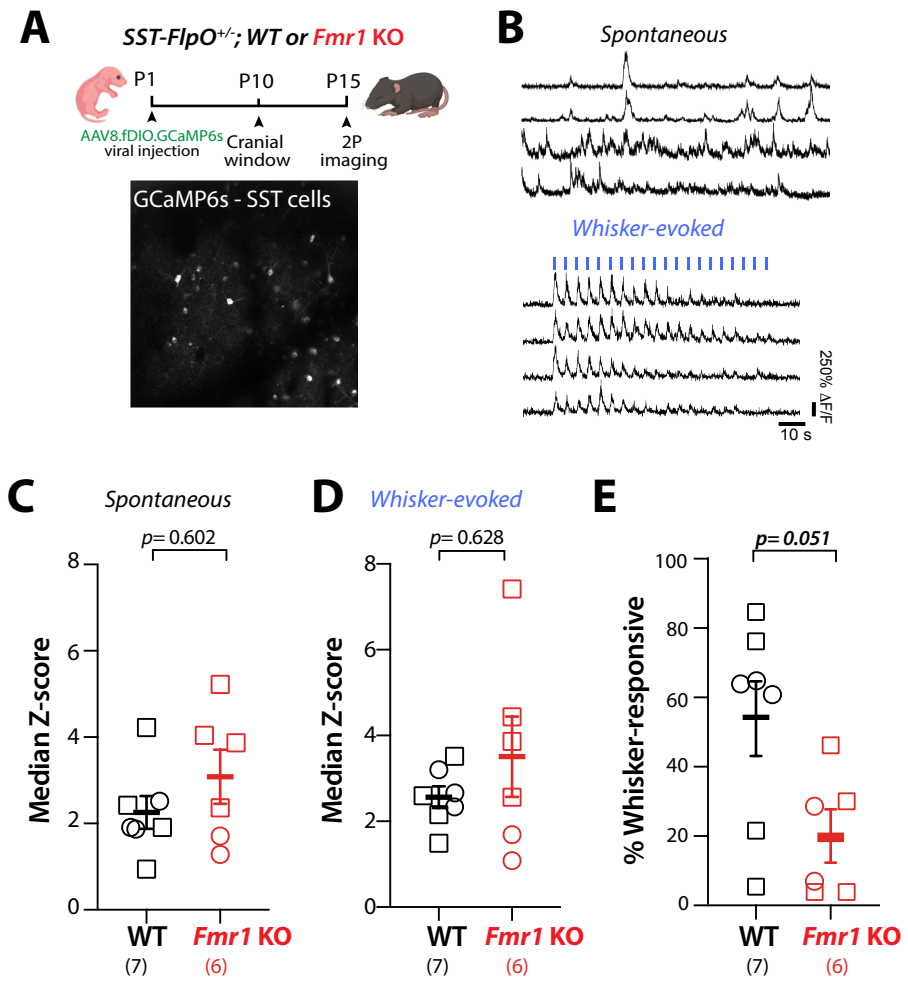

Supplementary Fig. S2

Supplementary Fig. S2: Activity of SST INs in S1 of P15 *Fmr1* KO mice is not different from WT controls. (Related to Fig. 1)

A. Top: Cartoon of experimental design for calcium imaging recordings in SST-INs. Bottom: Example field of view of SST-INs expressing GCaMP6s in SST-FlpO mice at P15.
B. Example traces of calcium transients for spontaneous and whisker-evoked activity in both SST-FlpO ; WT and SST-FlpO*; Fmr1* KO mice (we show traces from 2 different SST-INs of 2 different animals). The vertical blue bars represent the 20 whisker stimulations.
C. Mean Z-scores for spontaneous activity of SST-INs in *Fmr1* KO and WT mice at P15 (2.56± 0.38 for WT vs. 3.08± 0.62 for *Fmr1* KO, n=6 and 7 mice, respectively; p=0.602, MW t-test).
D. Mean Z-scores for whisker-evoked activity of SST-INs in *Fmr1* KO and WT mice at P15 (2.56± 0.25 for WT vs. 3.51± 0.94 for *Fmr1* KO, p=0.628, MW t-test).
E. Percentage of whisker-responsive SST-INs in *Fmr1* KO and WT mice at P15 (53.8± 11.0% for WT vs. 19.6± 7.6% for *Fmr1* KO, p= 0.051, M-W t-test).

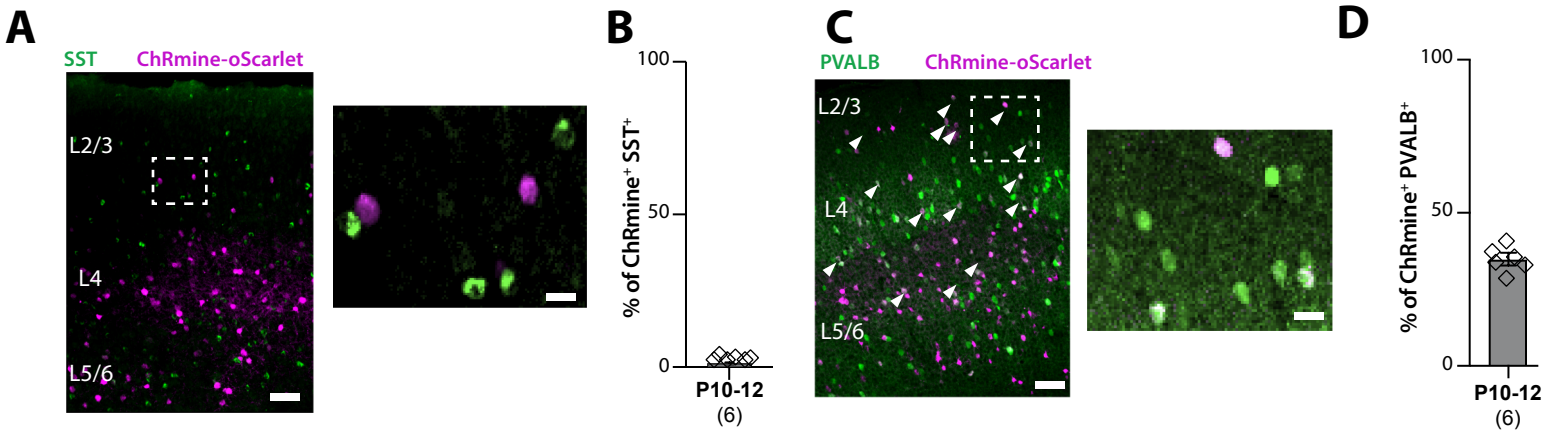

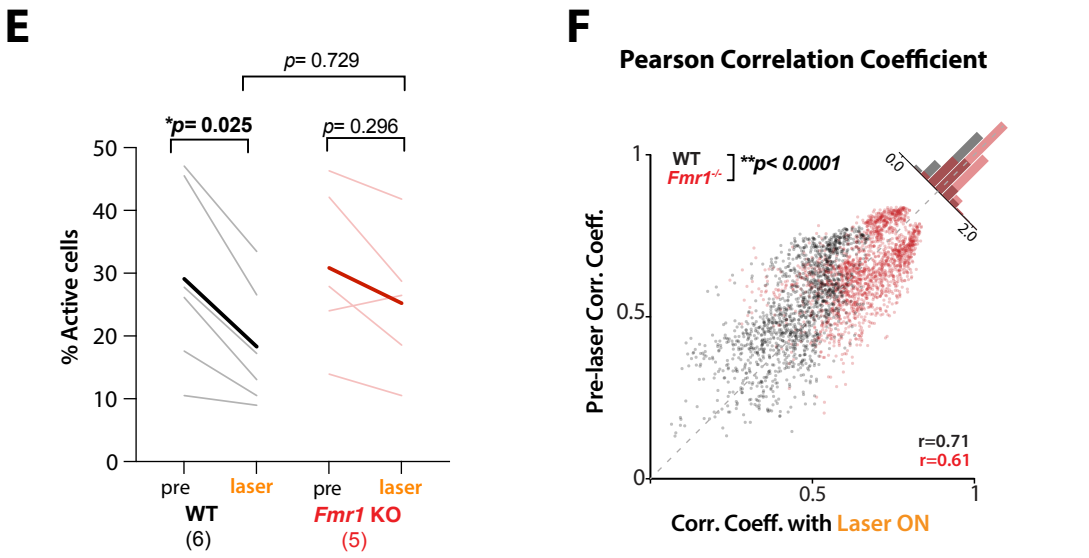

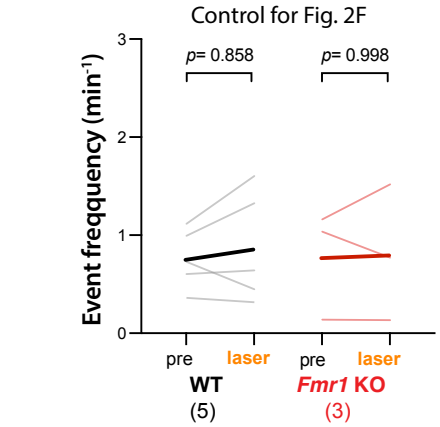

Supplementary Fig. S3

Supplementary Fig. S3: Controls for optogenetic experiments to stimulate Nkx2.1-INs in an attempt to modulate Pyr neurons in neonatal *Fmr1* KO mice at P10. (Related to Fig. 2)

A. Example field of view in S1 of Nkx2.1-Cre;Sst-FlpO*; Fmr1* KO expressing ChRmine (magenta), using AAV-EF1-CreON/FlpOFF-ChRmine-oScarlet- virus) and immunostained for SST (green).
B. Quantification of ChRmine^{+} cells that also express either PVALB or SST (by immunohistochemistry). As expected almost none of the ChRmine-labeled cells were SST immunoreactive (1.2± 0.4%, n= 6 mice), confirming the intersectional strategy worked as intended to target Nkx2.1^{+} but SST-FlpO^{+} cells at P10.
C. Example field of view in S1of Nkx2.1-Cre;Sst-FlpO*; Fmr1* KO expressing ChRmine (same as in b) and immunostained for SST (green). White arrowheads indicate double labeled cells.
D. Quantification of ChRmine^{+} cells that are also immunoreactive for PVALB. Overall, 34.9± 2.1% the ChRmine-labeled also expressed PVALB (n= 6 mice). This is consistent with the fact that at this developmental stage (P10-P12) not all future PV-IN have started expressing PVALB.
E. The percentage of active Pyr cells is significantly reduced upon laser stimulation of ChRmine-expressing future PV-INs in WT mice but is unchanged in *Fmr1* KO mice (29.1± 6.0 pre laser vs. 18.3± 4.0 laser On, p=0.025 in WT mice vs. 30.9± 5.9 pre laser vs. 25.2± 5.2 laser On in *Fmr1* KO mice, p=0.296, two-way ANOVA post-hoc Tukey).
F. Change in pairwise correlation coefficients after optogenetic Nkx2.1-IN activation in Nkx2.1-Cre;Sst-FlpO mice for individual pairs of neurons (Spearman r=0.71, n=1,449 neuron pairs from n=6 WT mice; Spearman r=.0.61, n=1,842 neuron pairs from n=5 *Fmr1*^{KO} mice). Note that correlation coefficients are significantly reduced by laser stimulation in WT mice, but not in *Fmr1* KO mice, as shown by the frequency distribution ($p<0.001$, Kolmogorov-Smirnov test).
G. Mean frequency of Pyr cell calcium transients remained unchanged upon optogenetic stimulation in Nkx2.1-Cre;Sst-FlpO WT and *Fmr1* KO mice that do not express the opsin ChRmine (mCherry controls; 0.67± 0.13 pre laser vs. 0.86± 0.25 laser On, p=0.312 in WT mice; 0.78± 0.32 pre laser vs. 0.81± 0.4 laser On, p=0.500, n=5 WT and n=3 *Fmr1* KO , two-way ANOVA, post-hoc Tukey).

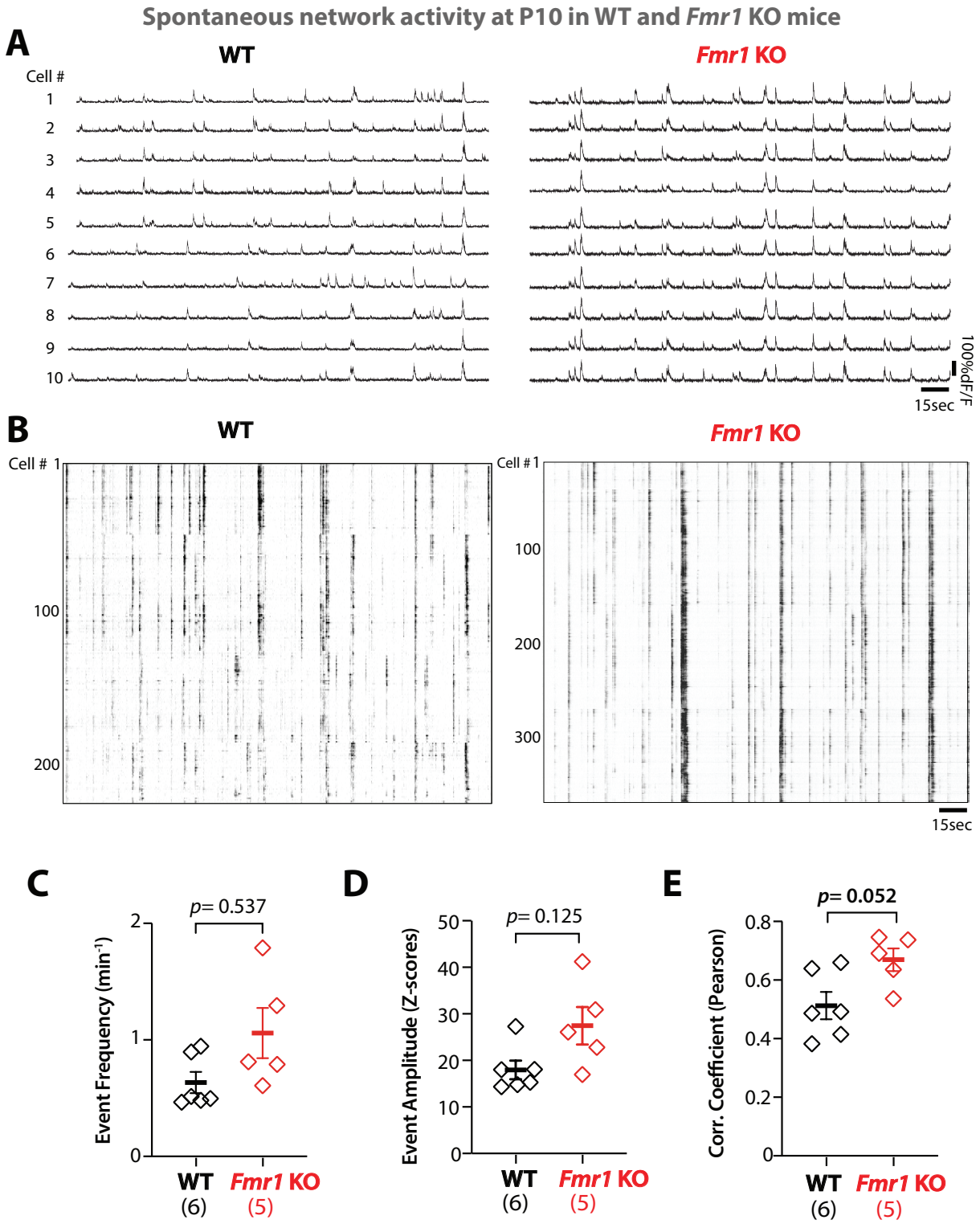

Supplementary Fig. S4

Supplementary Fig. S4: Pyr cell activity at P10 in *Fmr1* KO is hypersynchronous. (Related to Fig. 2)

A. Representative calcium traces of 10 example Pyr neurons in S1 of P10 WT and *Fmr1*^{KO}.
B. Raster plots of Pyr cell activity in a representative WT and *Fmr1* KO mouse. Note the higher synchrony of network *Fmr1* KO.
C. Mean frequency of Pyr cell calcium transients is not significantly different in WT and *Fmr1* KO mice (0.63± 0.09 in WT mice; 1.60± 0.21, n=6 WT and n=5 *Fmr1* KO mice, p=0.537 MW test).
D. Mean amplitude of Pyr cell calcium transients is not significantly different in WT and *Fmr1* KO mice (23.6± 2.00 in WT mice; 27.5± 4.0, n=5 WT and n=6 *Fmr1* KO mice, p=0.125, MW test).
E. Mean pairwise correlation coefficients is higher in *Fmr1* KO mice as compared to WT (0.51± 0.05 in n=6 WT mice; 0.67± 0.04, and n=5 *Fmr1* KO mice, p=0.052, MW test).

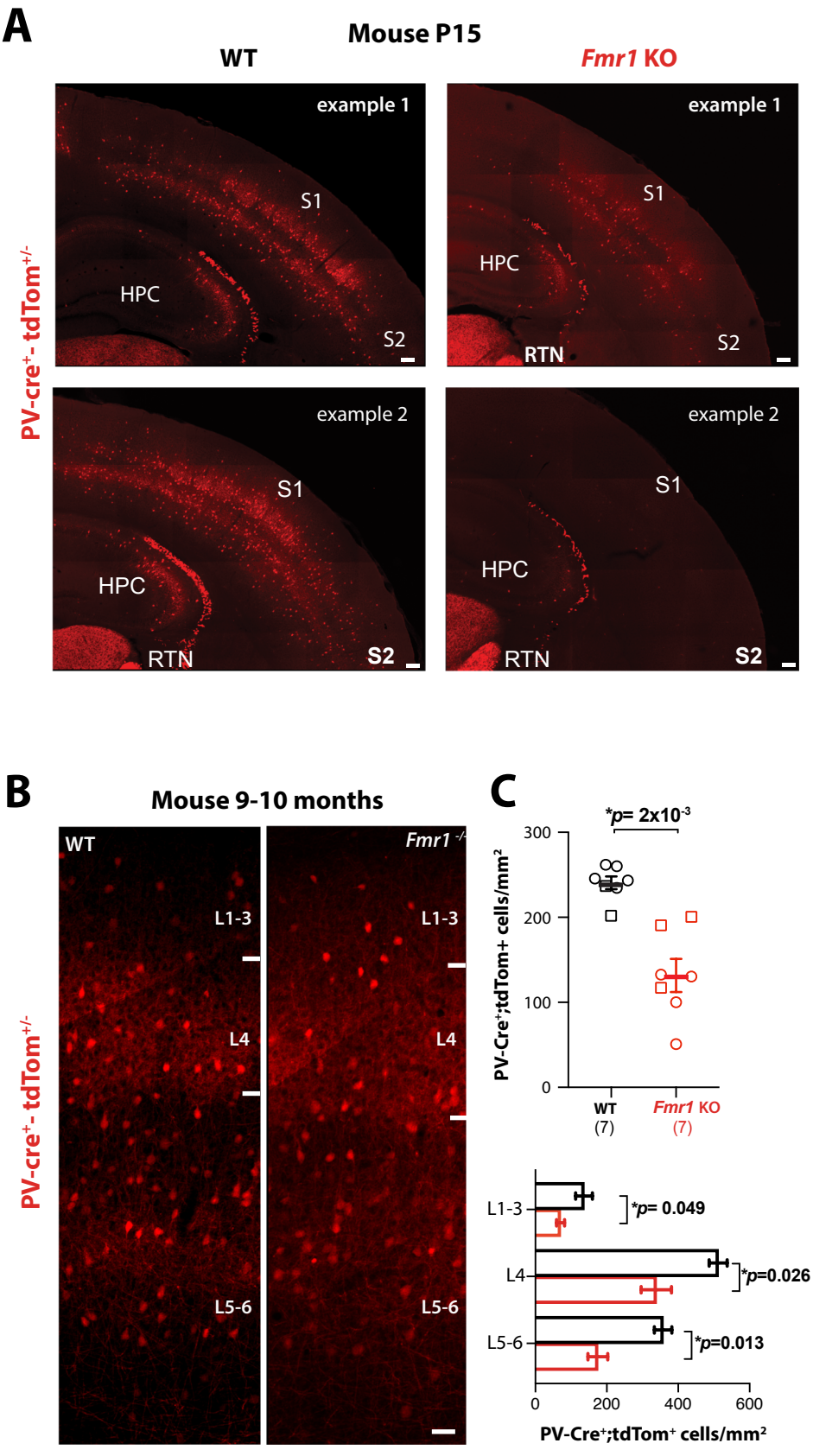

Supplementary Fig. S5

Supplementary Fig. S5: Reduced PV-IN density in *Fmr1* KO mice at P15 and at 9-10 months. (Related to Fig. 3)

A. Example coronal sections through S1 from *PV*-Cre;tdTom$^{+/-}$ mice (WT and *Fmr1*^{KO}) at P15 showing the range of PV-IN density in *Fmr1* KO mice across the dorsal brain. Notably some *Fmr1* KO mice (example 2) exhibit a dramatic loss of PV-INs in neocortex and hippocampus (HPC), while other bran regions, such as the reticular thalamic nucleus (RTN) are much less affected. S2: secondary somatosensory cortex. Scale=100 μm.

B. Coronal sections through the barrel field of S1 from PV-Cre;tdTom$^{+/-}$ mice (WT and *Fmr1* KO) at 9-10 months (corresponding approximately to age of human tissue in Fig. 3C-D). Scale= 50 μm.

C. Mean density of PV-tdTom^{+} INs in S1 is significantly lower in adult *Fmr1* KO mice (top), even across individual cortical layers (bottom). (all layers: 241± 8 cells/mm^2 for WT vs. 132± 2 for *Fmr1* KO; p=0.002, MW *t*-test; L2/3: 136± 23 vs. 69± 10, p=0.049, L4: 512± 26 vs. 339± 43, p=0.026; L5/6: 358± 24, two-way ANOVA, post-hoc Holm-Sidak test, p=0.013, n=7 per genotype).

SST-IN density in 15 day-old and adult WT and *Fmr1* KO mice

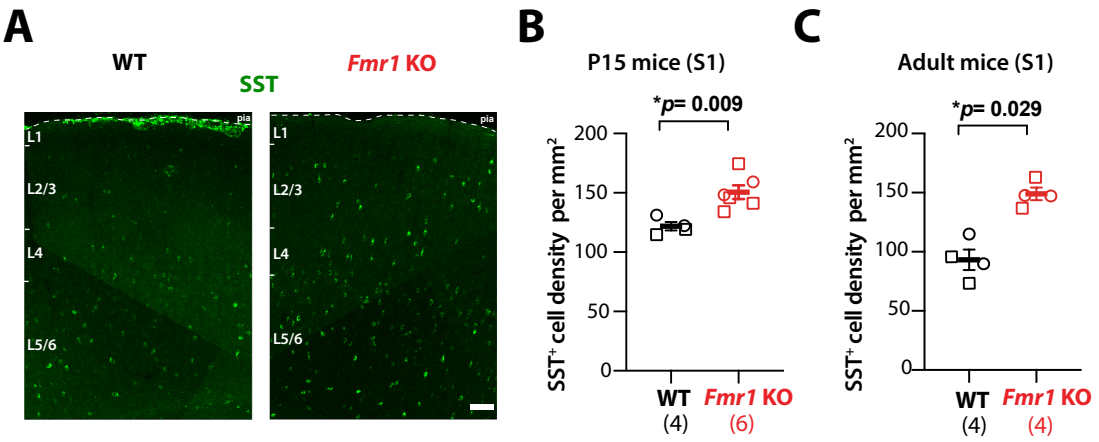

Density of Calretinin- and Calbindin-expressing interneurons subtypes in adult adult WT and *Fmr1*$^{-/-}$ mice

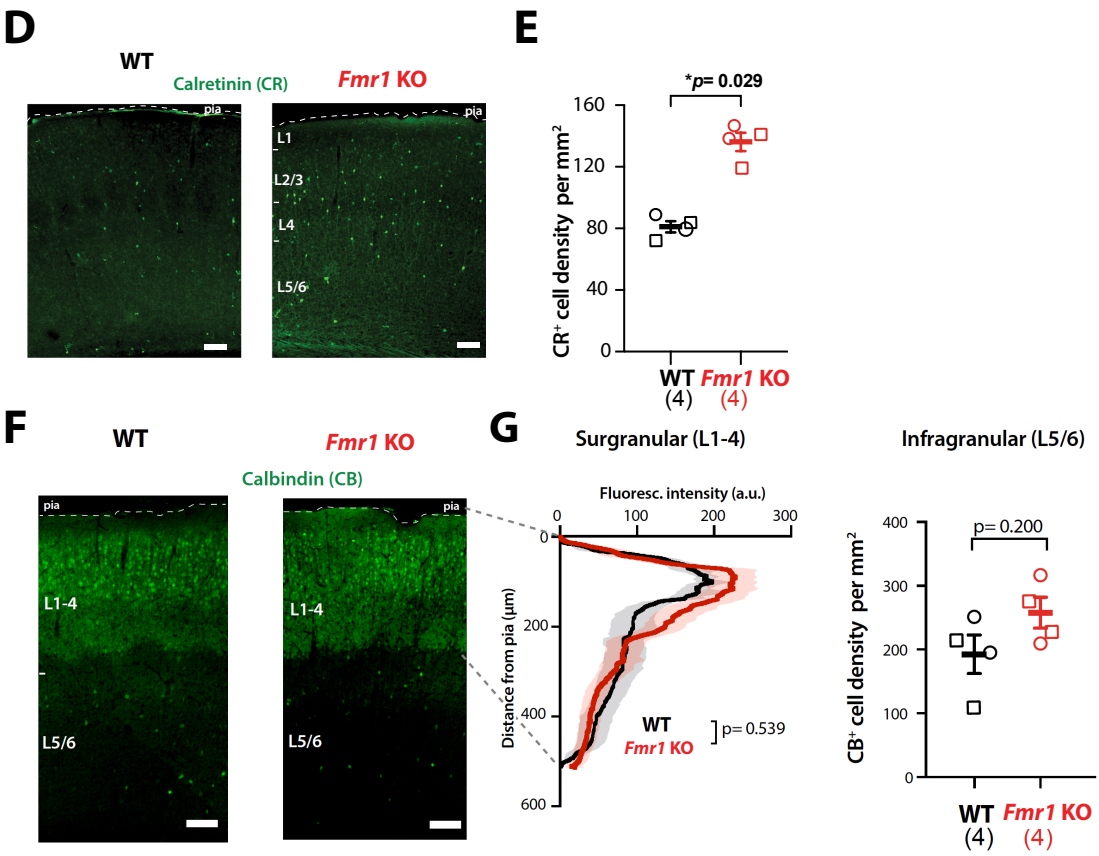

Density of Calretinin- and Calbindin-expressing interneurons in human samples

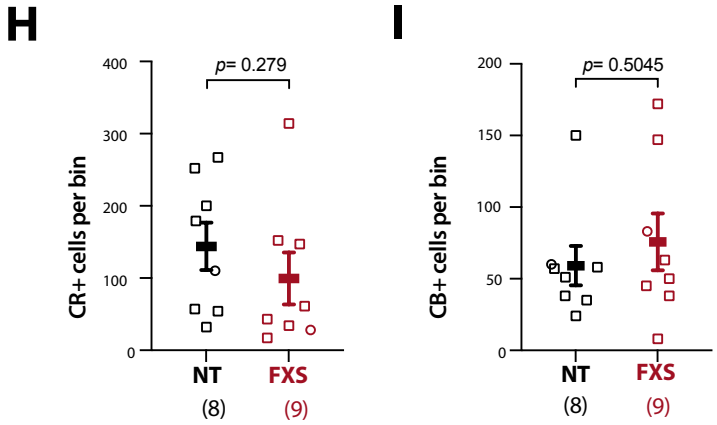

Supplementary Fig. S6

Supplementary Fig. S6: Density of SST, Calbindin, and Calretinin INs in FXS human cases and *Fmr1* KO mice. (Related to Fig. 3)

A. Representative images of SST immunostaining in S1 in P15 WT and *Fmr1* KO mice.
B. Quantification of total SST-immunoreactive cell density in the barrel field of S1 in WT and *Fmr1* KO mice in P15 (WT: 121.9± 3.7 cells/mm^2, *Fmr1* KO: 150.5± 5.9, n= 4 and 6, respectively; p=0.009, MW test).
C. Quantification of total SST-immunoreactive cell density in adult (4-5 months old) WT and *Fmr1* KO mice in and adult mice (WT: 93.14± 8.6 cells/mm^2, *Fmr1* KO: 149.1± 5.3, n= 4 per group; p=0.029, MW test)
D. Representative images of Calretinin immunostaining in S1 in adult WT and *Fmr1* KO mice.
E. Quantification of Calretinin-immunoreactive INs from adult WT and *Fmr1* KO mice (81± 3.6 for WT vs. 136± 5.9 for *Fmr1* KO, n=4 mice per group; p=0.029 MW *t* test).
F. Representative images of Calbindin immunostaining in S1 in adult WT and *Fmr1* KO mice. Note that the CB immunoreactivity is similar to previous reports. [2,3]
G. Quantification of Calbindin-immunoreactive INs in WT and *Fmr1* KO mice. The distribution and intensity of fluorescence is comparable in between WT and *Fmr1* KO mice in the supragranular layers (AUC= 48,036± 704 for WT vs. 42,093± 578 for *Fmr1* KO, n=4 mice per group; p=0.539, MW *t* test). The density of CB$^+$ INS in infragranular layers is similar between WT and *Fmr1* KO mice (192.6± 30.2 for WT vs. 257.7± 24.2 for *Fmr1* KO; p=0.200, MW *t* test).
H. Quantification of Calbindin-immunoreactive INs in human FXS and neurotypical control (NT) cases (59± 14 for NT vs. 76± 20 for FXS, n=8 and 9, respectively; p=0.279 MW *t* test).
I. Quantification of Calretinin-immunoreactive INs in FXS human and control (NT) cases (144± 33 for NT vs. 100± 36 for FXS; p=0.279 MW *t* test).

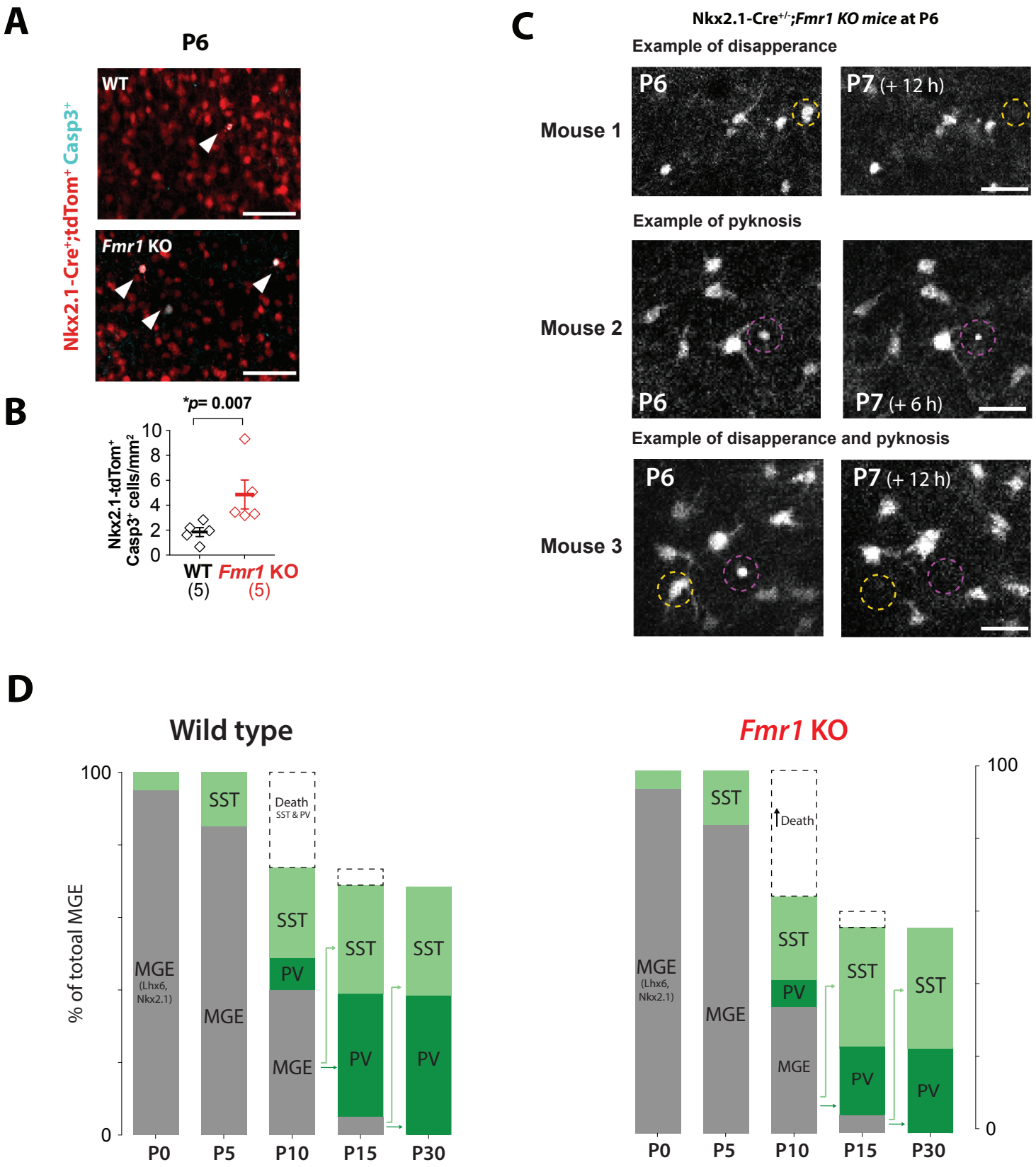

Supplementary Fig. S7

Supplementary Fig. S7: Evidence of apoptotic cell death of *Nkx2.1*-tdTom$^+$ INs in neonatal *Fmr1* KO mice. (Related to Fig. 3)

A. Coronal sections through S1 from *Nkx2.1-Cre* mice (WT and *Fmr1* KO) at P6 immunostained for cleaved Caspase-3 (cyan) showing rare double-labeled cells (arrowheads). Scale= 100 μm.

B. Mean density of Nkx2.1$^+$-tdTom$^+$-INs that co-express Caspase-3 was significantly higher in *Fmr1* KO mice (1.85± 0.35 cells/mm^2 for WT vs. 4.87± 1.16 for *Fmr1* KO; p=0.007, M-W test).

C. Representative maximum intensity projection (~20 μm) of *Nkx2.1*-tdTom$^+$ IN image stacks acquired by in vivo 2P microscopy of the same FOV at P6 and 6-12h later in 3 example *Nkx2.1-Cre;Ai14* $^{+/-}$; *Fmr1* KO mice. Yellow dotted contours indicate *Nkx2.1*-tdTom$^+$ INs present at P6 but absent at P7. Purple dotted contours indicate pyknotic Nkx2.1$^+$-tdTom$^+$-INs, indicative of apoptosis. Scale= 50 μm.

D. Cartoon representing developmental sequence of events related to differentiation of MGE-derived INs into SST and PV populations in WT (left) and *Fmr1* KO mice (right). Note that in WT mice, SST-INs differentiate before PV-INs, that naturally occurring cell death of SST-INs and PV-INs occurs roughly between P5 and P10, and that additional differentiation of PV-INs from MGE-derived precursors goes on after P15. In contrast, in *Fmr1* KO mice, there is 1. A lower density of PV-INs (due to an excess cell death), and 2. a higher density of SST-INs (presumably due to less cell death and/or greater differentiation from MGE-INs) compared to WT mice.

Chronic DREADD manipulation (P5 to P9)
in *Nkx2.1-Cre$^{+/-}$; WT or Fmr1* KO

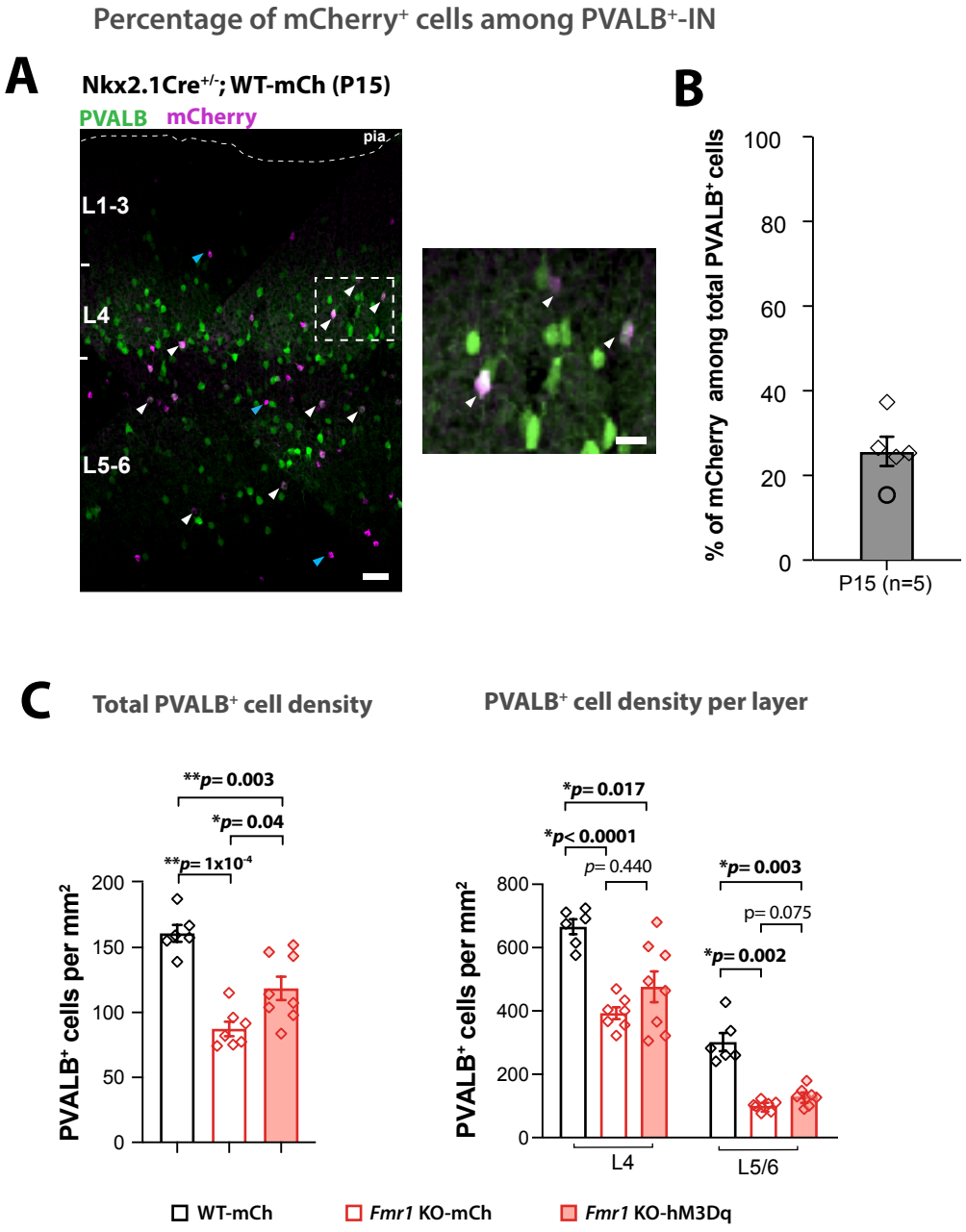

Supplementary Fig. S8

Supplementary Fig. S8: Chronic chemogenetic activation of Nkx2.1-INs (P5-P9) increases the density of PVALB$^+$ cells at P21. (Related to Fig. 4)

A. Coronal section through the barrel field of S1 in a P15 Nkx2.1-Cre;WT mouse expressing mCherry in Nkx2.1$^+$-IN (see Methods). Note the overlap in expression of mCherry (purple) in Nkx2.1$^+$-IN and PVALB immunoreactivity (green) across cortical layers (white arrowheads). As expected based on the low efficiency of viral transduction, only a small proportion of PVALB+ cells co-express mCherry (and the Gq DREADD construct) (blue arrowheads). Scale= 50µm.
B. Percentage of PVALB$^+$ INs that also express mCherry. (25.8± 3.5 cells/mm^2, n=5 mice).
C. Left: Quantification of PVALB+ INs density across cortical layers at P15. (161± 6 cells/mm^2 for WT-mCherry vs. 87± 6 for *Fmr1* KO-mCherry, p= 0.003; and 119± 9 for *Fmr1* KO-h3MDq, p= 0.040, n=6, 7 and 8, respectively). Right: the chronic DREADD manipulation did not significantly change the density of PV-INs in L4 or L5/6.

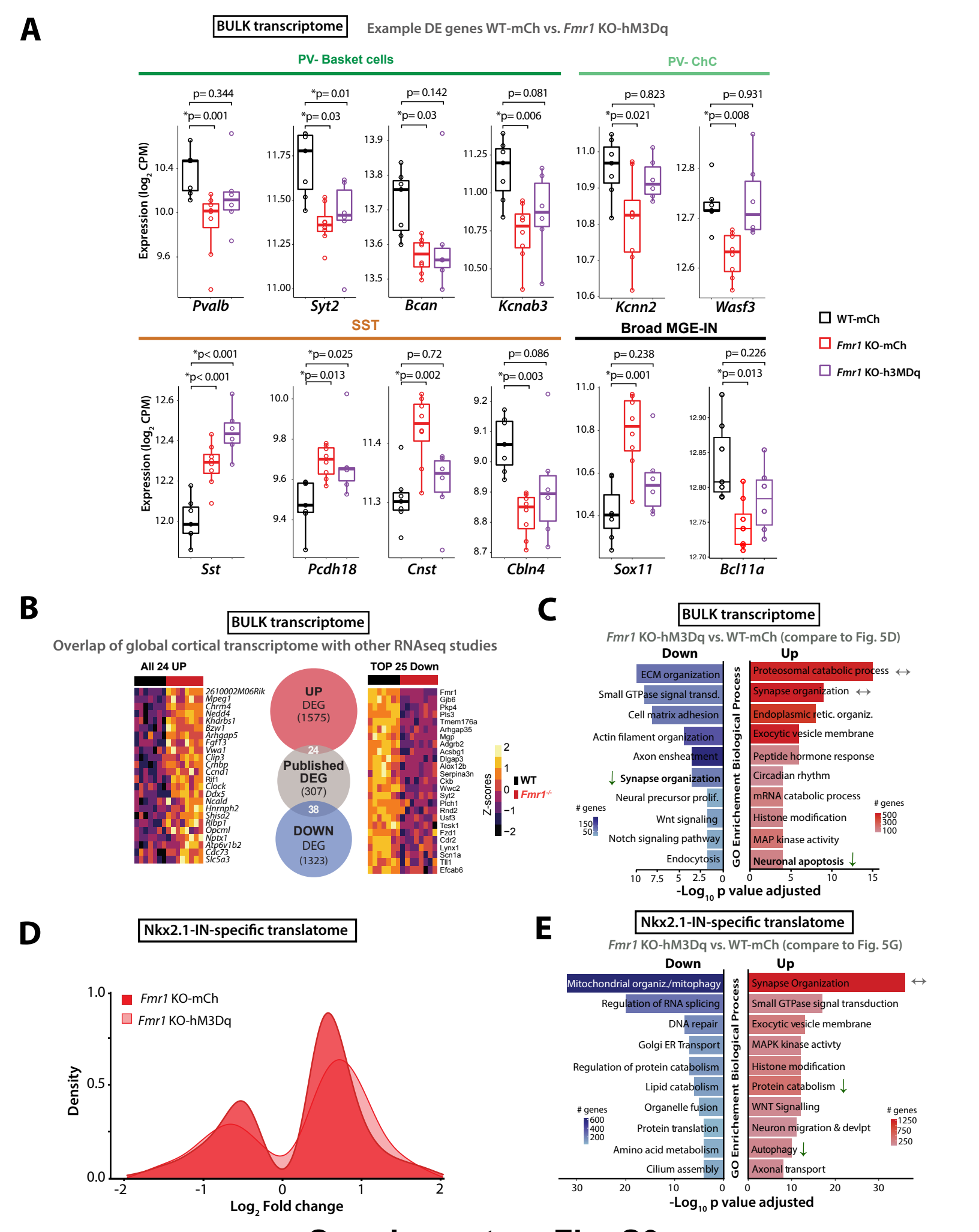

Supplementary Fig. S9

Supplementary Fig. S9: Gene ontology (GO) analysis for DE genes in *Fmr1* KO-hM3Dq mice compared to WT-mCherry mice, and effect of Gq DREADD manipulation. (Related to Fig. 5)

A. Whisker plots comparing the expression of several MGE-derived markers in the bulk transcriptome. Markers shown for PV-INs, including fast-spiking basket cells and chandelier cells, and SST-INs markers; Wilcoxon signed-rank test.
B. Number of DE genes in S1 cortex at P15 *Fmr1* KO-mCherry from the bulk transcriptome that overlap with previously reported differentially expressed in the hippocampus of adult *Fmr1* KO mice (see Methods). Heatmaps represent the changes of expression expressed as Z-scores among the up- and downregulated genes.
C. Top 10 GO terms (using the biological process package) enriched among downregulated (blue) and upregulated (red) genes from the bulk cortical transcriptome in *Fmr1* -hM3Dq vs. WT-mCherry mice. Scale bars represent the number of genes in each category. Note that "*Synapse organization*" and "*Neuronal apoptosis*" categories are less different (reduced number of genes and adjusted p value) than in the comparison shown in Fig. 5D between *Fmr1* KO (mCherry) and WT (mCherry) mice, suggesting they were 'improved' by the chemogenetic activation of Nkx2.1-INs.
D. Density plot showing how the $\log_2$ fold change was affected by the DREADD manipulation in the Nkx2.1-IN specific translatome. Note that differences with WT mice were accentuated by the DREADD intervention in both down- ad upregulated categories.
E. Top 10 GO terms for DE genes from the Nkx2.1-specific translatome in *Fmr1* KO -hM3Dq vs. WT-mCherry mice. Only a few GO terms were modestly improved by DREADDs (e.g., *Protein catabolism* and *Autophagy*).

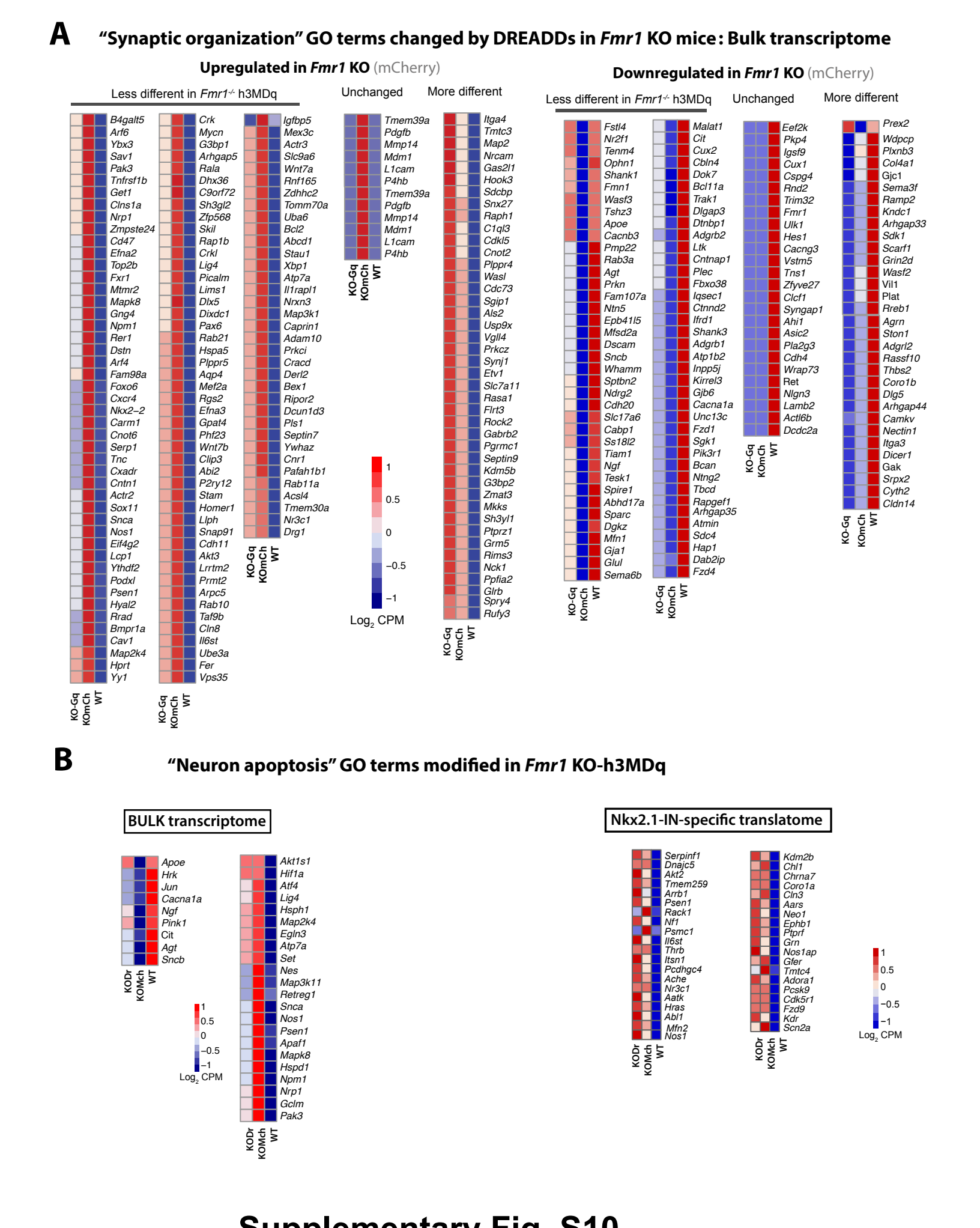

Supplementary Fig. S10

Supplementary Fig. S10: Gene expression levels changed by C21 treatment in *Fmr1* KO-hM3Dq mice. (Related to Fig. 6)

A. List of upregulated or downregulated genes among the GO term *Synapse organization* in *Fmr1* KO-mCherry and hM3Dq groups (as compared to WT-mCherry) within the bulk cortical transcriptome. Heatmaps represent the average for each treatment/genotype group in (log_2 CPM). Note that, while DREADD treatment reduced differences for many genes. The expression of other genes was either unhanged or worsened after C21 treatment.
B. Same as in panel A but for GO term "*Neuronal apoptosis*." In both bulk transcriptome (left) and Nkx2.1-IN specific translatome (right).

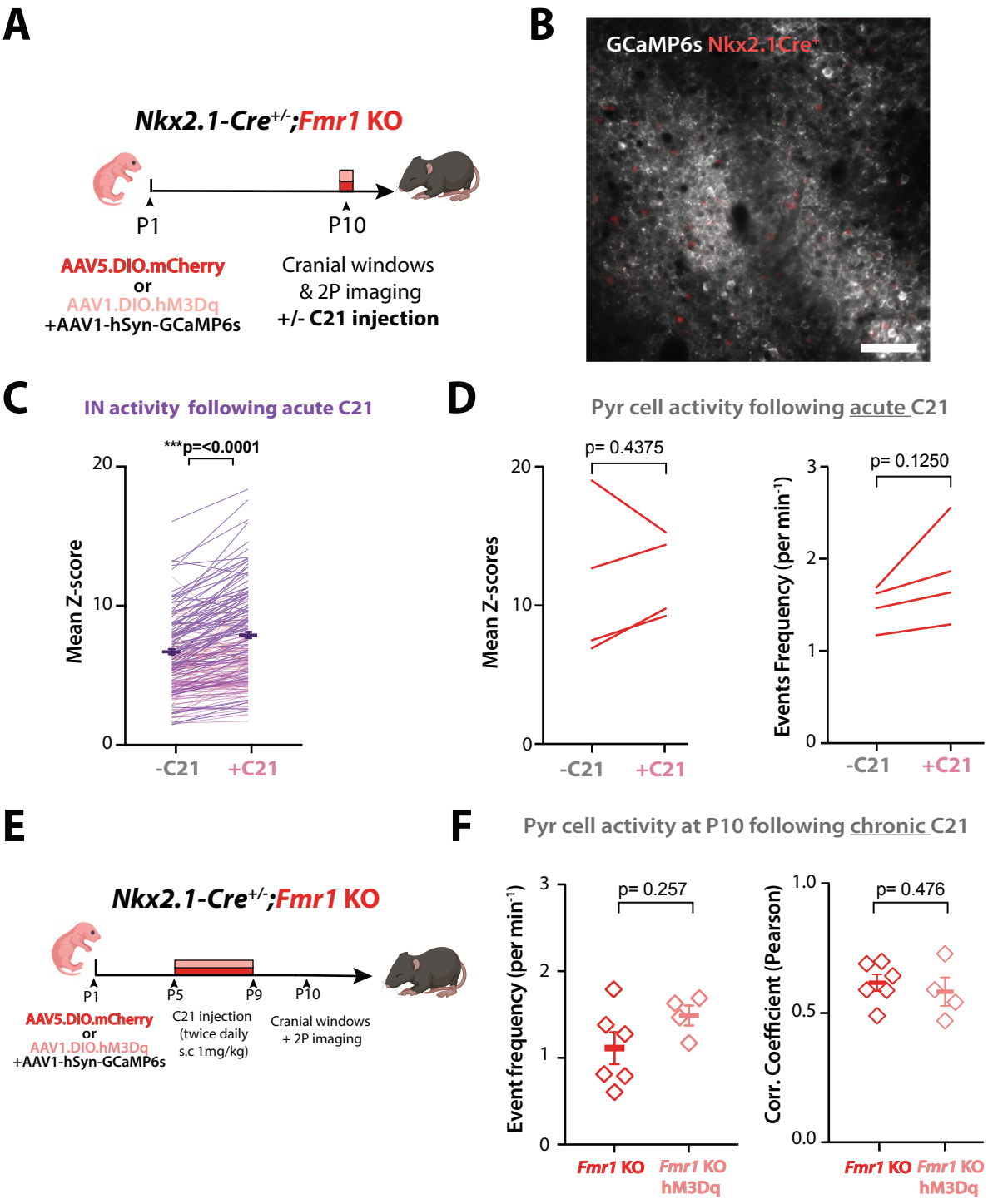

Supplementary Fig. S11

Supplementary Fig. S11: Acute chemogenetic activation of Nkx2.1-INs at P10 or chronic activation from P5 to P9, fails to modulate Pyr cell activity. (Related to Fig. 7)

A. Experimental design for acute chemogenetic activation of Nkx2.1-INs at P10 in *Fmr1* KO mice to assess cortical circuit activity using in vivo calcium imaging at P10.
B. Example FOV of Pyr cells expressing GCaMP6s and Nkx2.1-hM3Dq^{+} IN in S1 of *Nkx2.1-Cre; Fmr1* KO mouse (scale=100µm).
C. Mean Z-scores of Nkx2.1-INs before (-C21) and 30-40min after s.c. injection of C21 (+C21) in P10 *Fmr1* KO-hM3Dq mice. Mean activity of Nkx2.1-INs is significantly higher following C21 injection (-C21: 6.61± 0.19 and +C21: 7.83± 0.23, n= 182 cells from 3 mice; p<0.0001, Wilcoxon matched-pairs signed rank test).
D. Left: Mean Z-scores of Pyr cells before (-C21) and 30-40min after (+C21) s.c. injection of C21 (1mg/kg) in P10 *Fmr1* KO-hM3Dq mice. Acutely increasing the activity of Nkx2.1-INs had no effect on Pyr cell activity (-C21: 11.52± 2.82 and +C21: 12.16± 1.55, p=0.437, Wilcoxon matched-pairs signed rank test). Right: the mean frequency of synchronous network events (Pyr cells) remained unchanged after C21 in P10 *Fmr1* KO-hM3Dq mice. (-C21: 1.48± 0.11 and +C21: 1.83± 0.26 events/min, n= 4 mice; p=0.125, Wilcoxon matched-pairs signed rank test).
E. Experimental design for chronic chemogenetic activation of Nkx2.1-INs (from P5 to P9) in *Fmr1* KO mice to assess cortical circuit activity using in vivo calcium imaging at P10.
F. Left: Mean frequency of Pyr cell calcium transients at P10 was not significantly different *Nkx2.1-Cre; Fmr1* KO -hM3Dq mice after chronic C21 injections from P5 to P9 compared to *Fmr1* KO mice (1.11± 0.18 in *Fmr1* KO n=6 vs. 1.48± 0.11 events per min in *Fmr1* KO-hM3Dq mice n=4, p=0.257, MW test test). Right: Mean pair-wise correlation coefficients of Pyr cell calcium transients is unchanged in *Fmr1* KO-hM3Dq mice following chronic C21 injection from P5 to P9 (0.66± 0.03 in *Fmr1* KO n=6, and 0.62± 0.05 in *Fmr1* KO-hM3Dq mice n=4, p=0.476 MW test). Note that 1 animal was a new *Fmr1* KO-mCherry control, while the other 5 mice are *Fmr1* KO from Fig S4C-E.

Acute DREADD manipulation of PV-IN reduces spontaneous Pyr cell activity in P15 Fmr1 KO mice

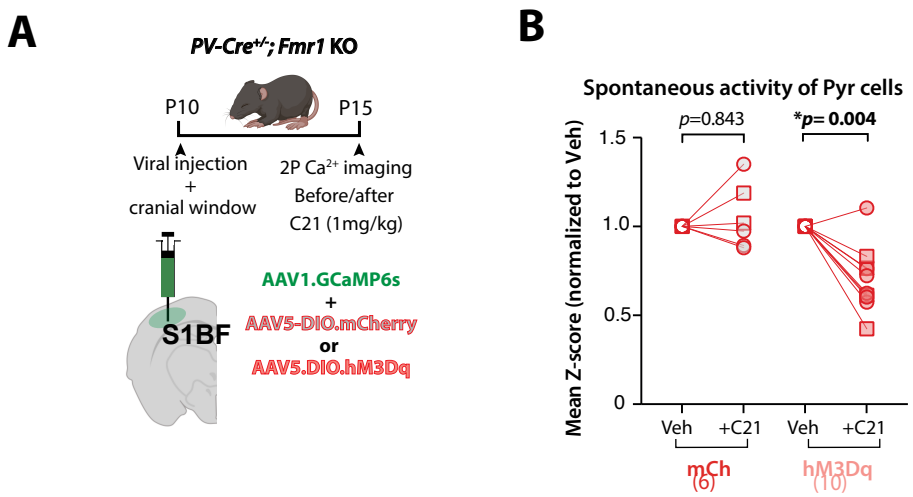

Acute optogenetic manipulation of MGE-IN reduces Pyr cell activity P15 Fmr1 KO mice

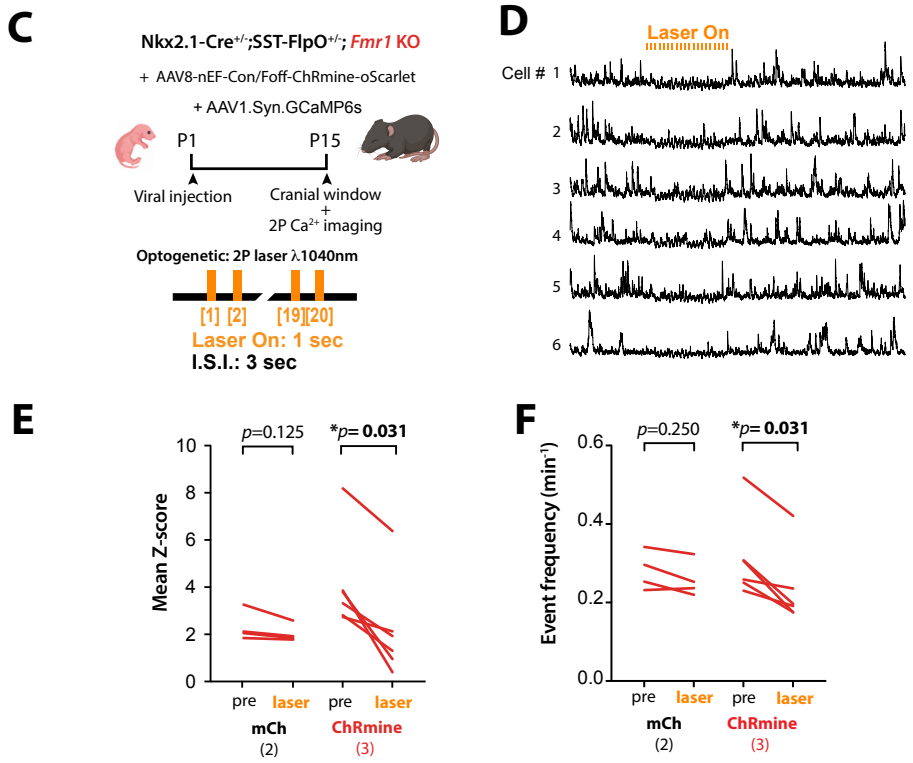

Acute DREADD manipulation of PV-IN modulates whisker-evoked responses

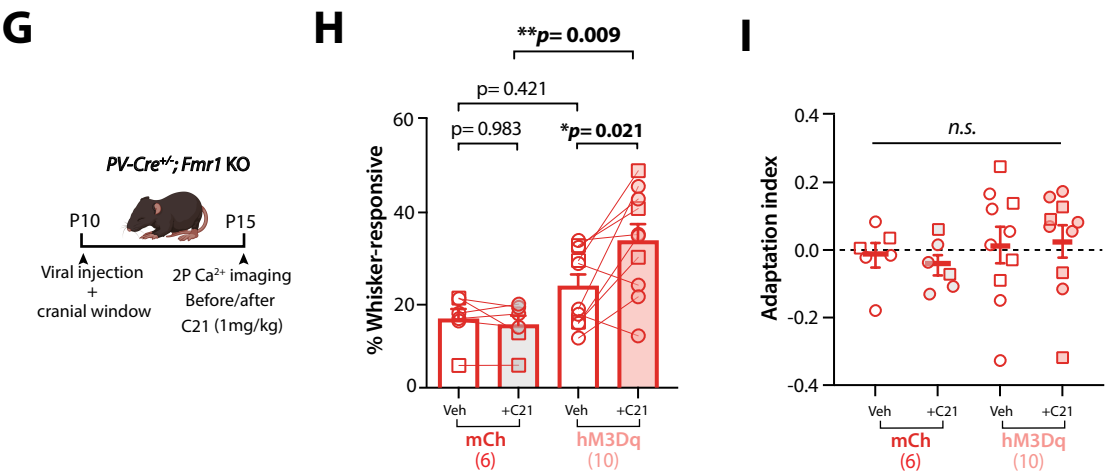

Supplementary Fig. S12

Supplementary Fig. S12: Acute chemogenetic or optogenetic activation of INs reduces Pyr cell activity at P15 in *Fmr1* KO mice. (Related to Figs. 7 and 8)

A. Experimental design for in vivo calcium imaging recordings in Pyr cells after acute chemogenetic activation of PV-INs at P15. Calcium imaging was performed at P15 before and 30-40min after s.c injection of C21.

B. Mean Z-score for spontaneous activity of L2/3 Pyr cells is reduced upon C21 injection in *Fmr1* KO -hM3Dq mice but not in *Fmr1* KO mCherry controls (before/after C21: 3.9± 0.7 vs. 4.0± 0.6 in mCherry group, p=0.843; and 2.3± 0.3 vs. 1.6± 0.3, p=0.004 in hM3Dq group; n=6 and 10 mice, respectively; Wilcoxon matched pair signed rank test).

C. Experimental design for optogenetic experiments. *Nkx2.1*-Cre mice (*Fmr1* KO or WT) were injected with a CreOn/FlpOff-ChRmine virus at P1 to express the opsin ChRmine in Nkx2.1-Cre^{+}; Sst-FlpO^{-} INs. Calcium imaging was done at P15 before, during, and after 20 laser pulses of orange light (1 s-long, 3 s I.S.I., λ=1,040 nm), just as in Fig. 2.

D. Representative calcium traces for 6 Pyr cells (black) upon 2P laser stimulation.

E. Mean Z-score of activity in Pyr cells before (pre) and during optogenetic stimulation (laser) in *Fmr1* KO mice. Each line in the panel represents an individual field of view. We observe a significant reduction of Pyr cell activity upon laser stimulation in ChRmine-expressing mice but not in control mCherry mice (2.32± 0.32 pre vs. 2.03± 0.18 with laser; p= 0.125; n=4 FOV from 2 control mice) ; 4.12± 0.83 pre vs. 2.18± 0.87 with laser; n=6 FOV from 3 ChRmine-expressing mice ; p= 0.019. Wilcoxon matched-paris signed rank test).

F. Mean event frequency of calcium transients of Pyr cells before (pre) and during optogenetic stimulation (laser) in P15 *Fmr1* KO mice. We observe a significant reduction of Pyr cell activity upon laser stimulation in ChRmine-expressing mice but not in control m-Cherry mice (0.28± 0.02 pre vs. 0.25± 0.02 with laser; p= 0.250 in control mice; 4.12± 0.83 pre vs. 2.18± 0.87 with laser for ChRmine-expressing mice; p= 0.031, Wilcoxon matched-pairs signed rank test).

G. Experimental design for calcium imaging recordings in Pyr cells after acute chemogenetic activation of PV-INs at P15 with the hM3Dq DREADD agonist C21 (same as Suppl. Fig. S12A-B).

H. The percentage of whisker-responsive Pyr cells at P15 was significantly higher in upon C21 injection in *Fmr1* KO-hM3Dq mice (n=10) but not in *Fmr1* KO mCherry controls (n=6). (hM3Dq group before/after C21: 23.5± 2.8% vs. 33.9± 3.9%; p=0.021; and mCherry group before/after C21: 15. 9± 2.3% vs. 14.5± 2.1%; p=0.983; two-way *ANOVA* with post-hoc Tukey).

I. Neuronal adaptation was not affected by the DREADD manipulation (mCherry group before/after C21: -0.02± 0.09 vs. -0.05± 0.03, hM3Dq group: 0.02± 0.05 vs. 0.03± 0.05, p>0.99; two-way *ANOVA* with post-hoc Tukey).

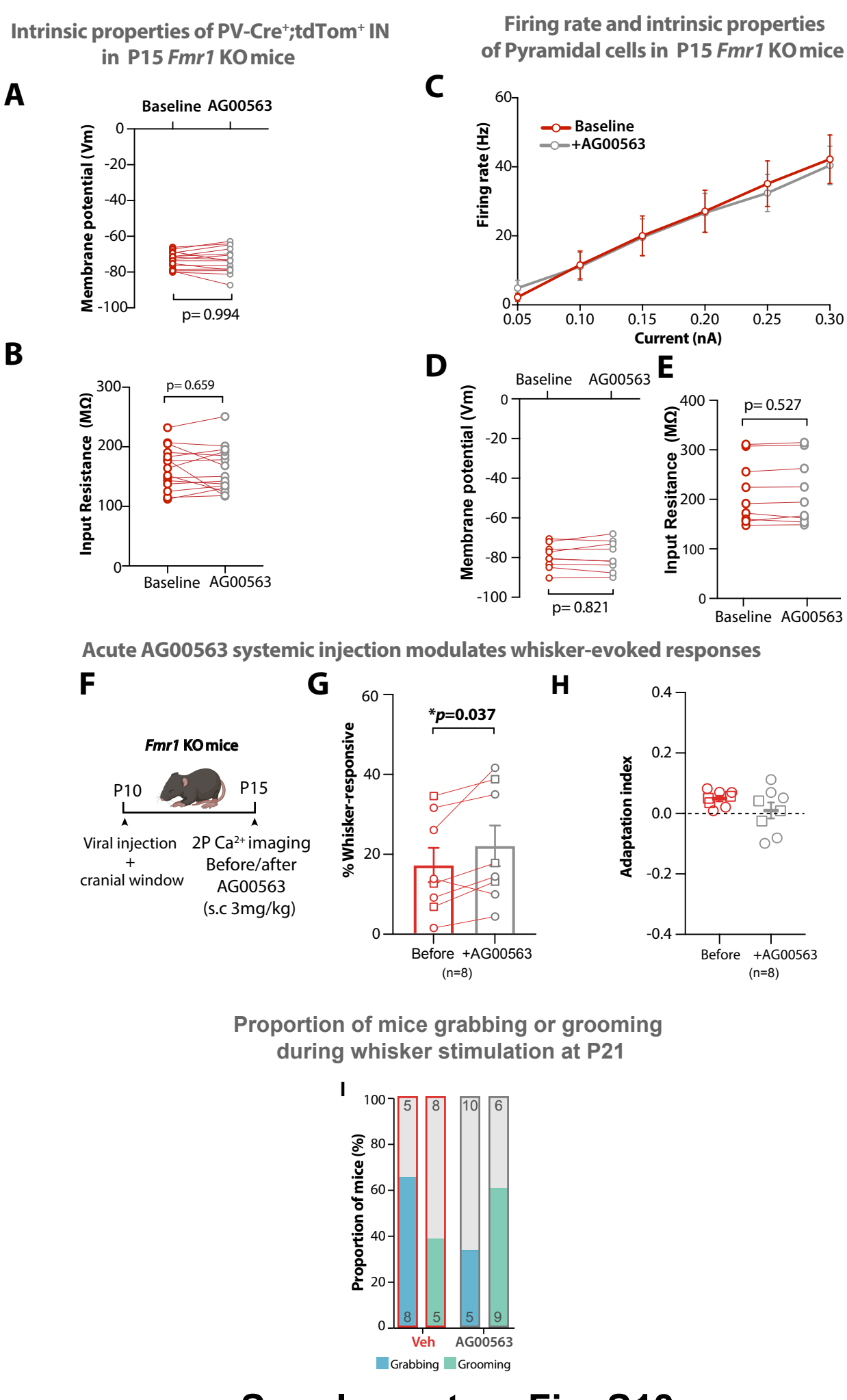

Supplementary Fig. S13

Supplementary Fig. S13: Intrinsic properties of PV-INs and Pyr cells are unchanged by AG00563 (and relative proportions of grabbing/grooming in AG00563 treated mice).

(Related to Fig. 8)

A. Resting membrane potential (Vm) of PV-INs is unchanged by bath application of AG00563 during current clamp recordings of *PV*-tdTom+ cells (-73.4± 1.2 mV vs. -73.2± 1.8 mV, p= 0.805, paired t-test, n=15 cells from 6 *Fmr1* KO mice at P15-16).
B. Input resistance (Rm) of PV-INs is unchanged by AG00563 (164.6± 9.2 MΩ vs. 161.2± 10.1 MΩ, p= 0.608, paired *t*-test).
C. Cumulative input-output curves during baseline (red) or bath application of AG00563 (gray) (n=9 Pyr cells from 6 PV-Cre;tdTom+/-;*Fmr1* KO mice, two-way RM ANOVA).
D. Vm of Pyr cells is unchanged by AG00563 (-79.5± 2.1 mV vs -79.3± 2.5 mV, p=0.805, paired t-test).
E. Rm of Pyr cells is unchanged by AG00563 (214.0± 21.4 MΩ vs. 215.4± 22.0 MΩ, p=0.608, paired *t*-test).
F. Experimental design for the acute administration of AG00563 (3 mg/kg, s.c.) and calcium imaging at P15, before and 30 min after injection.
G. The percentage of whisker-responsive Pyr cells in *Fmr1* KO mice was significantly higher after AG00563 injection compared to baseline (17.1± 4.3% baseline vs. 21.9± 5.1% ~30-40 min after AG00563, p=0.033; paired t-test, n=8 mice).
H. The neuronal adaptation index of Pyr cells was not changed by AG00563 (0.05± 0.01 baseline vs. 0.01± 0.03 after AG00563, p=0.033; paired t-test, n=8 mice).
I. A smaller percentage of mice showed defensive behavior (grabbing) at least once during whisker stimulation in the AG00563-treated group than among vehicle controls (5/15 mice vs. 8/13, respectively). The opposite was true for adaptive healthy behavior (grooming) (9/15 mice vs. 5/13, respectively).

Case ID	Sex	Age	PMI (Hours)	Diagnosis	CGG Repeat Count	Hemisphere	Cause of Death
UCD 14-15	M	60	80	Control	NA	Right	Pulmonary Emboli
UCD 18-05	M	62	37	Control	NA	Left	Cardiopulmonary Arrest
UCD 15-07	F	64	NK	Control	NA	Left	NK
UCD 18-07	M	65	240	Control	NA	Left	Cardiac Arrest
UCD 14-01	M	66	48.5	Control	NA	Right	Acute Renal Failure
UCD 18-08	M	68	168	Control	NA	Left	Hypoxic Respiratory Failure
UCD 14-12	M	68	NK	Control	NA	Left	Cardiac Arrest
UCD 19-12	M	81	72	Control	NA	Left	NK
1031-08-GP	M	57	20	FXS	436	Left	Multiple System Organ Failure
1031-09-LZ	M	64	11.5	FXS	429	Left	NK
1061-19-JB	F	64	30	FXS	629,780	Left	NK
1005-14-JC	M	65	60	FXS	600-700	Right	Congestive Heart Failure
1013-10-SK	M	76	NK	FXS & FXTAS	447,540	Left	Respiratory Failure
1001-18-LD	M	78	6	FXS	235	Right	NK
1033-08-WS	M	79	17.5	FXS		Left	NK
1007-18-RF	M	80	NK	FXS	1,000	Right	NK

Table S1. Clinical characteristics of postmortem neurotypical and Fragile X cases.
(Related to Figure 3).
(NK: not known; NA: not applicable; M: male; F: female; PMI: post-mortem interval; FXS: Fragile X syndrome; FXTAS: Fragile X-associated tremor/ataxia syndrome).

SUPPLEMENTAL VIDEOS

Supplementary video 1 (Related to Fig. 2). Example of in vivo calcium imaging of Pyr cells before, during, and after optogenetic stimulation of presumed future PV-IN s in Nkx2.1-Cre;SST-Flp$^{+/-}$ mice at P10. Data was acquired at 15 fps and is played back at 2x speed.

Supplementary video 2 (Related to Fig. 4). Example of in vivo calcium imaging of Pyr cells during whisker-evoked activity in Nkx2.1-Cre mice at P2. Data was acquired at 15 fps and is played back at 1x speed.

References

1. Che, A., Babij, R., Iannone, A.F., Fetcho, R.N., Ferrer, M., Liston, C., and García, N.V.D.M. (2018). Layer I Interneurons Sharpen Sensory Maps during Neonatal Development. Neuron *99*, 98-116.e7. 10.1016/j.neuron.2018.06.002.

2. Nigro, M.J., Hashikawa-Yamasaki, Y., and Rudy, B. (2018). Diversity and Connectivity of Layer 5 Somatostatin-Expressing Interneurons in the Mouse Barrel Cortex. Journal of Neuroscience *38*, 1622–1633. 10.1523/jneurosci.2415-17.2017.

3. Daigle, T.L., Madisen, L., Hage, T.A., Valley, M.T., Knoblich, U., Larsen, R.S., Takeno, M.M., Huang, L., Gu, H., Larsen, R., et al. (2018). A Suite of Transgenic Driver and Reporter Mouse Lines with Enhanced Brain-Cell-Type Targeting and Functionality. Elsevier Inc. *174*, 465-480.e22. 10.1016/j.cell.2018.06.035.